Research Square

Preprints are preliminary reports that have not undergone peer review.
They should not be considered conclusive, used to inform clinical practice,
or referenced by the media as validated information.

Automatic detection of thermal fusion joints defects of high-density polyethylene gas pipes using ultrasonic total focusing method and deep learning

Tianliang Chen
China Jiliang University
Qiang Wang
qiangwang@cjlu.edu.cn

China Jiliang University
Quanjing Xiao
Engineering China Jiliang University
Hong Wang
Huzhou Special Equipment Inspection Center
Yanlei Liu
Hangzhou Special Equipment Inspection Science Research Institute

Research Article

Keywords: Defect detection, deep learning, phase coherence factor, polyethylene pipe, thermal fusion joints, total focus imaging

Posted Date: November 21st, 2024

DOI: https://doi.org/10.21203/rs.3.rs-5395473/v1

License: This work is licensed under a Creative Commons Attribution 4.0 International License.
Read Full License

Additional Declarations: No competing interests reported.

Automatic detection of thermal fusion joints defects of high-density polyethylene gas pipes using ultrasonic total focusing method and deep learning

Tianliang Chen[1], Qiang Wang[1*], Quanjing Xiao[2], Hong Wang[3], Yanlei Liu[4]

1. *College of Energy Environment and Safety Engineering, China Jiliang University, Hangzhou, Zhejiang, 310018, China.*
2. *College of Mechanical and Electrical Engineering，China Jiliang University, Hangzhou, Zhejiang, 310018, China.*
3. *Huzhou Special Equipment Inspection Center, Huzhou, Zhejiang, 313099, China.*
4. *Hangzhou Special Equipment Inspection Science Research Institute, Hangzhou, Zhejiang,310051, China.*

[*] Corresponding author.

E-mail addresses: qiangwang@cjlu.edu.cn(Q.Wang).

Abstract

Inspection of thermal fusion joints is essential for in-service high-density polyethylene (HDPE) gas pipe operating safety. A directivity-compensated circular coherence factor weighted total focusing method (D-CCF-TFM) algorithm is presented to solve the problem of low imaging quality of phased array ultrasonic testing during inspecting thermal fusion joints of HDPE pipes. The D-CCF-TFM leverages the circular coherence factor (CCF) to reduce noise interference during calculating the phase of defect and employs a directivity function to compensate sound field intensities in different directions, leading to obvious average signal-to-noise ratio (SNR) improvement compared to TFM, as confirmed through experiments on thermal fusion joint and test block. To automate defect detection in D-CCF-TFM images, an improved YOLOX algorithm is proposed, incorporating a convolutional block attention module (CBAM) and adopting the complete intersection over union (CIoU) as the regression loss. Evaluation of this improved YOLOX algorithm on a dataset of 2504 images yielded a mean average precision (mAP) of 99.15%, demonstrating its effect in detecting small defects. Thus, it provides theoretical and technical support for quality detection of thermal fusion joint welding.

Keywords Defect detection, deep learning, phase coherence factor, polyethylene pipe, thermal fusion joints, total focus imaging.

1 Introduction

High-Density Polyethylene (HDPE) pipes are widely utilized as the primary material for gas transmission in urban medium and low-pressure gas pipe networks due to their exceptional corrosion resistance, structural attributes, and economic feasibility [1,2]. Welding defects in thermal fusion joints pose a critical factor in failures, which can lead to serious safety accidents such as gas leakage [3]. It is imperative to employ reliable and precise non-destructive evaluation (NDE) techniques for detecting and characterizing defects in thermal fusion joints. Microwave technology has been employed to detect embedded defects in HDPE materials [4], however, the detection of smaller-sized defects remains

challenging. Infrared thermography images, on the other hand, do not enable the detection of deep defects [5], limiting comprehensive defect assessment. While X-ray imaging reveals the internal features of the sample [6], high cost and radiation damage to the human body hinder its practical application.

Phased array ultrasonic testing (PAUT) has been demonstrated significant potential in the examination of HDPE materials [7,8], but its imaging performance for small defects and out-of-focus anomalies remains suboptimal. The total focusing method (TFM), derived from full matrix capture (FMC), is a widely adopted PAUT imaging technique [9]. It has a growing application in the NDE of composite materials [10,11]. However, the viscoelasticity of HDPE materials has been caused severe attenuation of ultrasonic waves during imaging inspection, resulting in a decrease in the amplitude of the echo signal. This impacts the imaging quality of the TFM algorithm.

In ultrasonic NDE, due to superior phase stability in defect generated signals contrasted with background noise, the phase information of ultrasonic signal can be used for imaging to reduce the impact of amplitude loss on imaging quality. Camacho et al. [12,13] proposed the phase coherence imaging (PCI) algorithm, it is accomplished by extracting the instantaneous phase of the signal, calculating the phase difference between defects and noise, and constructing a phase coherence factor (PCF) matrix to weigh the amplitude of each pixel in the image, thereby suppressing structural noise. Ge et al [14] employed the circular coherence factor (CCF) with time reversal (TR) weighted TFM algorithm to suppress structural noise in concrete ultrasonic inspections. Tian et al. [15] used the PC-weighted -TFM imaging method to detect defects in CFRP, and the results showed that the interlayer reflection was suppressed, and the imaging signal-to-noise ratio (SNR) was improved. J. Camacho et al. [16] used the combination of Sign Coherence Image (SCI) and TFM to evaluate the crack state with high accuracy. Gauthier et al [17] employed vector coherence factor (VCF) to detect defects in grooving of 20 mm thick cold-rolled steel plates. The combination of PCF and TFM method for defect detection has been well applied. However, the sound field of ultrasonic array has its own directivity, the directivity radiation energy of ultrasonic array at different angles is different, resulting in different intensity of sound field at different positions in the imaging results which affects the quality of imaging. It has been shown that compensating the directivity of sound field can reduce ultrasonic attenuation in materials to a certain extent [18-19]. However, there is currently a lack of research on the use of the directivity of sound field to improve the PCF. This presents an opportunity for detecting defects in HDPE materials.

The primary objective of enhancing the signal-to-noise ratio (SNR) is to facilitate clear recognition of defects in ultrasonic images by inspectors. However, extensive training for inspectors can be costly and may lead to errors when handling a large volume of images. Consequently, the development of automated defect detection technology has become essential [20-21]. Hasanian et al. [22] employed an artificial neural network optimized by a random genetic algorithm for defect image detection. Li et al. [23] used an optimized SVM to identify defective images of polyethylene gas pipelines.

With the rapid advancement of deep learning technology, particularly convolutional neural networks (CNN), their application in PAUT images recognition has become widespread. Medak et al. [24] utilized an EfficientDet-D0 model based on CNN architecture for automated defect detection in PAUT images of stainless steel samples with various types of defects. In [25], the application of YOLOv3 and SSD networks in detecting defects in PAUT images of steel blocks was introduced for the first time; however, they only employed 98 images for network training, which constitutes a limited sample size. Gantala and Balasubramaniam [26] utilized the YOLOv4 model for the automatic identification of weld defects in carbon steel TFM images, incorporating finite element simulation and DCGAN for image data augmentation. Shi et al. [27] have investigated defect identification in phased array ultrasonic inspection

images of HDPE pipe electrofusion joints using a CNN model. An YOLOX [28] model has also been used for defect detection in similar applications. However, there is a lack of research on defect detection of HDPE pipe thermal fusion joints images by using deep learning method.

In this paper, to solve the problem of low imaging quality and defect detection efficiency of HDPE thermal fusion joint, the D-CCF-TFM is proposed, and the directivity compensation factor is established according to the directivity function of the sound field to compensate the CCF, then weighted with the pixel amplitude in the TFM algorithm. The imaging quality of HDPE thermal fusion joint defects can be obtained, and its effectiveness is verified by experiments. Meanwhile, an YOLOX model is adopted to automatically detect defects in thermal fusion joint images, and improved the detection ability of the model by adding attention module and improving loss function. In addition, transfer learning is adopted to train the model, and the model is compared and evaluated. Finally, thermal fusion joints inspection experiments were carried out to verify the correctness of the proposed D-CCF-TFM.

2 Methodology

2.1 D-CCF-TFM Algorithm

The TFM imaging algorithm divides the imaging area into multiple grids and uses delay and sum (DAS) on the acquired FMC data to identify internal defects within the material using the calculate amplitude information. As shown in Fig. 1, for a given focal point $F(x,z)$, the flight time $t_{ij}(x,z)$ of an ultrasonic wave from emitting array element i to the focal point and then reflected back to the receiving array element j can be expressed by the following equation (1).

$$t_{ij}(x,z)=\frac{\sqrt{(x-x_i)^2+z^2}+\sqrt{(x-x_j)^2+z^2}}{c} \tag{1}$$

where c is the ultrasonic velocity in the sample, x_i represents the emitting array element central horizontal coordinate, x_j represents the receiving array element central horizontal coordinate.

[insert **Fig. 1**]

Fig. 1 Schematic diagram of TFM imaging method.

According to the TFM algorithm, the amplitude of a focus point within the imaging region can be determined, for a given focus point $F(x,z)$, its amplitude $I_{\mathrm{TFM}}(x,z)$ is represented by equation (2).

$$I_{TFM}(x,z)=\sum_{i=1}^{N}\sum_{j=1}^{N}h(S_{ij}(t_{ij}(x,z))) \tag{2}$$

where N is the number of array elements, S_{ij} is the ultrasonic echo signal emitted by the i array element and received by the j array element, $h(x_i,x_j,t_{ij})$ is the Hillbert transform with the expression.

$$h(x_i,x_j,t_{ij})=h(\cos(\varphi)+j\sin(\varphi)) \tag{3}$$

where, φ is the phase angle of the $F(x,z)$,$|h|$ is the mode of the signal.

Phase coherence uses the phase difference between defective and non-defective regions during ultrasonic propagation to accurately locate and image defects. The circular coherence factor (CCF) [12,13]is used to characterize the phase distribution of the signal, and then the weight matrix is constructed, which can avoid the amplitude loss of the ultrasonic signal at the defect and effectively suppress the noise at the same time, the $CCF(x,z)$ can be calculated as:

$$CCF(x,z)=1-\sqrt{var(\cos\varphi(x,z))+var(\sin\varphi(x,z))} \tag{4}$$

where *var* is the variance, the expression for *var*(cos$\varphi(x,z)$) is given by:

$$var(\cos\varphi(x,z)) = \frac{1}{N^2}\sum_{i=1}^{N}\sum_{j=1}^{N}(\cos\varphi(x,z))^2 - (\frac{1}{N^2}\sum_{i=1}^{N}\sum_{j=1}^{N}\cos\varphi(x,z))^2 \tag{5}$$

while the expression for *var*(sinφ) is:

$$var(\sin\varphi(x,z)) = \frac{1}{N^2}\sum_{i=1}^{N}\sum_{j=1}^{N}(\sin\varphi(x,z))^2 - (\frac{1}{N^2}\sum_{i=1}^{N}\sum_{j=1}^{N}\sin\varphi(x,z))^2 \tag{6}$$

The directivity function [19] reflects the relationship between the energy of the sound field and the propagation direction of the sound beam. It balances the energy difference of the sound beam in different directions and compensates for the sound field intensity of the array elements at different angles. This compensation can effectively reduce the imaging error caused by ultrasonic attenuation. Therefore, a directivity-compensation factor *D* is established based on the directivity function of the array element in the sound field. For a one-dimensional linear array, the directivity compensation factor $D(x,z)$ can be determined as follows:

$$D(x,z) = D(\omega,\theta) = \mathrm{sinc}\left[\frac{(\sin\theta)\cdot a_0\cdot\pi}{\lambda}\right] \tag{7}$$

where the expression for sinc(x) is expressed by:

$$\mathrm{sinc}(x) = \frac{\sin(\pi x)}{\pi x} \tag{8}$$

where, λ is the ultrasonic wavelength; ω is the frequency, θ is the angle from the array element to an arbitrary $F(x,z)$, α_0 is the width of the array element.

The directivity compensation factor $D_{ij}(x,z)$ for a pair of emitting and receiving array element combinations (where array element *i* emitting and array element *j* receives) is the product of the directivity of the emitting and receiving array elements in the sound field. This can be expressed by the following equation (9).

$$D_{ij}(x,z) = \mathrm{sinc}\left[\frac{(\sin\theta_{iF})\cdot a_0\cdot\pi}{\lambda}\right]\mathrm{sinc}\left[\frac{(\sin\theta_{jF})\cdot a_0\cdot\pi}{\lambda}\right] \tag{9}$$

where, θ_{iF}, θ_{jF} are the angles from array element *i* and array element *j* to the $F(x,z)$, the schematic diagram of θ_{iF}, θ_{jF} angle is shown in Fig. 1.

The $D_{ij}(x,z)$ is then multiplied by the circular coherence factor *CCF* to obtain the directivity-compensated phase coherence factor *D-CCF*(x,z) as followed.

$$D\text{-}CCF(x,z) = D_{ij}(x,z)\cdot CCF(x,z) \tag{10}$$

The *D-CCF-TFM* is weighted with the $I_{\mathrm{TFM}}(x,z)$ to obtain the focal point amplitude $I_{\text{D-CCF-TFM}}$ of the directivity-compensated circular coherence factor weighted total focusing method algorithm, as shown in equation (11).

$$I_{\text{D-CCF-TFM}}(x,z) = D\text{-}CCF(x,z)\cdot I_{\mathrm{TFM}}(x,z) \tag{11}$$

2.2 Deep Learning Architecture

The objective of defect detection in thermal fusion joints is to locate and categorize anomalies in

images accurately. This can be achieved using deep learning-based object detection. There are two main types of models for this purpose. Two-stage detection models, such as Faster R-CNN [29], utilize candidate region generation, followed by classification and regression algorithms for target location. One-stage detection models, like YOLO and SSD, employ regression methods for direct mapping between input images and target boxes, enabling fast detection by predicting box locations and probabilities. YOLOX, an advanced model in the YOLO series, improves feature extraction network architecture to expand the network's receptive field. This advancement enhances the detection of small targets in images.

The YOLOX model consists of three integral components: the backbone, the neck, and the head. Upon introduction of an image into the backbone, it undergoes a process of feature extraction utilizing structural elements such as the Focus structure and CBS component, in conjunction with processes including CSPL and SPP. This results in the generation of three feature maps of differing dimensions. These feature maps then progress to the neck network where they are interconnected and undergo feature fusion via UpSampling and DownSampling techniques, culminating in the creation of a feature pyramid that accumulates semantic information at an advanced level. The fused feature maps derived from this phase are subsequently fed into the head network, thereby enabling multi-scale target detection capabilities.

However, defects of different sizes are often randomly dispersed in ultrasonic images of thermal fusion joints, which increases the complexity of defect identification in the network. As the depth of the network increases, the possibility of critical information being lost when detecting defects with low pixel ratios increases, resulting in misidentification. Therefore, two improvements were made to the YOLOX model, and the improved YOLOX architecture is shown in Fig. 2.

[insert **Fig. 2**]

Fig. 2 The improved YOLOX architecture

(1) Attention Module

The Convolutional Block Attention Module (CBAM) consists of two integral components: the Channel Attention Module (CAM) and the Spatial Attention Module (SAM). In the CAM, the input feature map F is initially subjected to global max and average pooling operations along its width and height dimensions. The resulting one-dimensional pooled vectors are then fed into a multilayer perceptron (MLP). Through the application of a sigmoid function, normalized channel attention weights are derived. Ultimately, these weights are multiplied with the input F to compute the channel attention-adjusted feature map F'. Subsequently, the SAM takes the F' feature map as its input. In this module, global max and average pooling operations are performed on F' based on its channels. The pooled channels are concatenated and passed through a convolutional layer utilizing a 7x7 convolutional kernel. The spatial attention weights are finally generated via a sigmoid function, which are then multiplied with the F' feature map to obtain the final feature map F''.

(2) Loss Function

The loss function regulates the predicted box's position by calculating the gap between the predicted box and the real box to improve the accuracy and localization of the YOLOX network prediction results. It comprises object loss, classification loss and regression loss. The regression loss uses Intersection over Union (IoU) to compute loss values that reflect the overlap ratio between the predicted box and the real box.

$$\mathrm{IoU} = \frac{|A \cap B|}{|A \cup B|} \tag{12}$$

Where: A is the predicted box, B is the real box, $A \cap B$ represents the area of its intersection, and $A \cup B$ represents the area of its concurrency.

To address the shortcomings of IoU loss concerning localization and prediction, this paper employs the Complete Intersection over Union (CIoU) [30] for the model. The CIoU introduces additional information, such as the box's center point and aspect ratio, leading to a more accurate assessment of the similarity between the predicted box and the ground truth box. It offers superior guidance for network learning, thereby resulting in enhanced detection precision and improved convergence speed. The calculation formula for the CIoU is presented as follows:(13) - (14).

$$\mathrm{CIoU} = \mathrm{IoU} - \left(\frac{\rho^2(b, b^{\mathrm{gt}})}{c^2} + \alpha\upsilon\right) \tag{13}$$

where the expression for α is given by:

$$\alpha = \frac{\upsilon}{(1 - \mathrm{IoU} + \upsilon)} \tag{14}$$

while the expression for υ is given by:

$$\upsilon = \frac{4}{\pi^2}\left(\arctan\frac{w^{\mathrm{gt}}}{h^{\mathrm{gt}}} - \arctan\frac{w}{h}\right)^2 \tag{15}$$

where: b is the center coordinate parameter of the prediction box; b^{gt} is the center coordinate parameter of the real box; ρ denotes the Euclidean distance between the two, and c is the length of the diagonal of the outer rectangle of the real box and the predicted image; w^{gt}, h^{gt} are the width and height of the real box; w, h are the width and height of the predicted box; α is the weight coefficient; and υ is the similarity of the aspect ratio.

3 Experiments and Analysis of D-CCF-TFM

3.1 Specimen and Experimental setup

To validate the effectiveness of the proposed D-CCF-TFM imaging method, we prepared two HDPE samples. The first specimen was a HDPE test block with a size of 400 mm × 40 mm × 80 mm. In the right area of the specimen block (A), φ1 mm, φ2 mm, and φ3 mm transverse through-hole defects were machined, and in the left area of the specimen block (B), φ1 mm transverse through-hole defects were machined, as shown in Fig. 3(a). The second specimen under consideration is a thermal fusion joint, as shown in Fig. 3(b) and Fig. 3(c), with an outer diameter of 315 mm and a thickness of 28.6 mm. This joint incorporates holes with diameters of φ2 mm, φ3 mm, and φ4 mm, each possessing depths of 6 mm, 10 mm, and 20 mm, respectively. Furthermore, it encompasses grooves measuring 2 mm × 4 mm, 3 mm × 7.5 mm, and 4.5 mm × 9 mm, which are strategically positioned at varying angles across the cross-sectional area. In addition, we obtained specimens of in-service HDPE thermal fusion joints, as shown in Fig. 3(c), to increase the sample size for subsequent defect detection.

[insert **Fig. 3**(a)]

[insert **Fig. 3**(b)]

[insert **Fig. 3**(c)]

Fig. 3 Test specimens of HDPE (a) test block(b)-(c) thermal fusion joint.

The experimental setup was shown in Fig. 4. It includes a TFM data acquisition instrument

(sampling frequency of 62.5 MHz), a ultrasonic transducer (central frequency of 2.25 MHz, 64 array elements, and an element spacing of 0.75 mm), a hand-held encoder. The inspection was conducted in the primary longitudinal wave mode with a velocity setting of 2300m/s.

[insert **Fig. 4**]

Fig. 4. Experimental setup.

3.2 Experimental Results and Discussion

The HDPE samples were scrutinized utilizing the previously described experimental setup and imaged through TFM, CCF, and D-CCF-TFM algorithms. Fig. 5 shows the imaging inspection results of the 1mm through-hole defect in the test block, and Fig. 6 and Fig. **7** show the imaging inspection results of the 2mm hole and 3mm×7.5mm groove in the thermal fusion joint, respectively.

The inspection results show that all three algorithms have been able to identify the location of the defects. As can be seen from Fig. 5, for the 1mm transverse through-hole defect in the test block, the PCI algorithm cannot detect defects at depths below 35mm and increases clutter amplitude above the image. The D-CCF-TFM algorithm effectively suppresses clutter above the image, while the imaging amplitude of the D-CCF-TFM algorithm is slightly reduced. Nevertheless, the fringe clutter around the defects is well suppressed. In Fig. 6(a) and Fig. 7(a), for defects in thermal fusion joint samples, the TFM algorithm introduces a large amount of structural noise in the detection image, as well as obvious scattered noise and artifacts around the defects. This leads to greater interference near the near-field region of the probe, thus affecting the accuracy of defect detection. In Fig. 6(b) and Fig. 7(b), the CCF algorithm suppresses clutter in the central area of the detection image and reduces the amplitude of the bottom echo to some extent. However, this results in an increase in clutter amplitude in the near-field area and a decrease in defect amplitude at greater depths. As shown in Fig. 6(c) and Fig. 7(c), the D-CCF-TFM algorithm effectively suppresses clutter in the upper and middle regions of the detected image. Although the amplitude of defects may be slightly reduced, clutter around the defect region is well suppressed, making defects easier to distinguish. The resolution of the detected image is also higher than that of the other two algorithms.

[insert **Fig. 5**(a)]

[insert **Fig. 5**(b)]

[insert **Fig. 5**(c)]

Fig. 5 Φ1 mm through-hole defect imaging inspection diagram of test block using (a) TFM (b) CCF (c) D-CCF-TFM.

[insert **Fig. 6**(a)]

[insert **Fig. 6**(b)]

[insert **Fig. 6**(c)]

Fig. 6 Φ2 mm hole defect imaging inspection diagram of thermal fusion joints using (a) TFM (b) CCF (c) D-CCF-TFM.

[insert **Fig. 7**(a)]

[insert **Fig. 7**(b)]

[insert **Fig. 7**(c)]

Fig. 7 3 mm x 7.5 mm groove defect imaging inspection map of thermal fusion joints using (a) TFM (b) CCF (c) D-CCF-TFM.

Fig. 8 presents the error curves of defect detection results. In Fig. 8(a), which depicts the defect width size detection error curve, the D-CCF-TFM algorithm and TFM algorithm exhibit more closely

fitting error curves compared to the CCF algorithm, which displays a larger undulation in its error curve. The average detection error for the TFM algorithm is within 0.92 mm, while the D-CCF-TFM algorithm demonstrates an average detection error within 0.74 mm. In Fig. 8(b), which depicts the defect depth size detection error curve, the error curves of the three algorithms are relatively proximal to one another. The detection error of the TFM algorithm is found to be within 1 mm, whereas the detection error of the D-CCF-TFM algorithm is confined within 0.86 mm. Overall, the detection accuracy of the D-CCF-TFM algorithm is higher than that of the other two algorithms.

To conduct a comprehensive and quantitative analysis of the imaging performance of each algorithm, we employed signal-to-noise ratio (SNR) and array performance index (API) as comparative metrics. Lower values of the *API* indicate superior resolution in defect imaging.

$$SNR = 20\lg\frac{I_{max}}{I_{average}} \tag{16}$$

$$API = \frac{A_{-6dB}}{\lambda^2} \tag{17}$$

Where: I_{max} is the maximum amplitude at the defect and $I_{average}$ is the average amplitude in the non-defective region. A_{-6dB} is the imaging area in the image where the amplitude decreases by 6 dB from the maximum value, and λ is the ultrasonic wavelength.

As can be seen in Fig. 8(c), the SNR of the CCF algorithm does not exhibit a substantial improvement compared to the TFM algorithm. Conversely, the imaging SNR ratio of the D-CCF-TFM algorithm demonstrates a marked enhancement, with an average increase of 9.43 dB relative to the TFM algorithm and 9.31 dB in comparison to the CCF algorithm. As can be seen in Fig. 8(d), both the CCF and D-CCF-TFM algorithms exhibit higher Array Performance Index (API) values compared to the TFM algorithm; however, the average API value of the D-CCF-TFM algorithm is slightly elevated by 3% relative to that of the CCF algorithm. This observation can be attributed to the reduction in the overall magnitude of the pixel-point matrix as the degree of weighting increases, which leads to the suppression of both noise and the magnitude of certain defective regions. Despite this, the D-CCF-TFM algorithm demonstrates superior performance when evaluated in terms of combined signal-to-noise ratio (SNR) and API values, surpassing both the CCF and TFM algorithms.

[insert **Fig. 8**(a)]

[insert **Fig. 8**(b)]

[insert **Fig. 8**(c)]

[insert **Fig. 8**(d)]

Fig. 8 Plots of the three imaging algorithms (a) width (b) depth and (c) SNR (d)API.

4 Experiment of Automatic Defect Detection

4.1 Dataset

The raw data for deep learning training is derived from the D-CCF-TFM algorithm images obtained as described in Section III. To enhance the accuracy and robustness of the model, the original dataset is augmented through random rotation, contrast enhancement, and the addition of noise. However, a challenge arises due to the fact that the imaging results of two different samples are not consistently identical in size. Although the training model interpolates image scaling, unifies sizes, and performs other operations, these procedures can potentially introduce distortions in the image, leading to

information loss and inaccuracies in the results. To address this issue, this study employs the sliding window method to extract image segments, with a clipping window size of 256 × 256 pixels. Furthermore, the dataset is constructed using a total of 2504 local images, which include 677 grooves and 1827 holes. The dataset is subsequently divided into a training set (80%) and a test set (20%) for the purpose of model development and evaluation.

4.2 Model Training

Windows 10 operating system was used for model training. The YOLOX network, which offers standardized architectures, can be classified into four distinct configurations: 's', 'x', 'm', and 'l', based on the network depth and the number of parameters. Considering factors such as the size of the training set and the constraints of the actual experimental conditions, the 's' variant was chosen for model training in this investigation to ensure a balance between computational efficiency and detection accuracy.

Due to the limited defect image data available for HDPE pipe thermal fusion joints, the training process is prone to overfitting, which can lead to poor model generalization. To mitigate this issue, a transfer learning strategy was employed during the model training phase. The parameters from the backbone feature extraction network of the original model, pretrained on a large classification dataset, were utilized as initial weights for the model. This methodology enhanced both the training efficiency and the network's feature extraction capabilities. The training process was divided into two distinct phases: the freezing phase and the unfreezing phase. For a detailed description of the specific parameters used in these phases, please refer to Table 1.

[insert **Table 1**]

Table 1 The parameters of model training

The loss value curves of the model are depicted in Figure 10. As shown in Fig. 9(a), the YOLOX model exhibits a substantial loss value, with the validation loss (Val loss) stabilizing after approximately 200 epochs, whereas the training loss (Train loss) continues to decrease, suggesting overfitting during the training process. In contrast, Fig. 9(b) presents the Train loss curve for the enhanced YOLOX model. Both the Train loss and Val loss demonstrate a steady decline, exhibiting a more harmonized trend. Notably, the Train loss consistently remains higher than the Val loss, which signifies an optimal state where the network has been adequately trained without overfitting.

[insert **Fig. 9**(a)]

[insert **Fig. 9**(b)]

Fig. 9 Loss Curves of Model Training: (a) YOLOX and (b) improved YOLOX.

4.3 Model Evaluation

To evaluate the detection performance of the model, we employed four key assessment metrics: precision (P), recall (R), mean average precision (mAP), and frames per second (F_{ps}). P is the proportion of correctly detected defects among all predicted defects, can be derived from equation (18).

$$P = \frac{T_{\mathrm{P}}}{T_{\mathrm{P}} + F_{\mathrm{P}}} \tag{18}$$

R indicates the proportion of actual defects that are successfully identified by the model, can be derived from equation (19).

$$R = \frac{T_{\mathrm{P}}}{T_{\mathrm{P}} + F_{\mathrm{N}}} \tag{19}$$

The mean Average Precision (mAP) integrates precision and recall across various confidence thresholds. It is calculated using a standard threshold commonly adopted in object detection tasks, specifically an IoU threshold of 0.5, as derived in Equation (20).

$$mAP@0.5 = \frac{1}{n}\sum_{1}^{n} AP_n @ \text{IoU}=0.5 \tag{20}$$

where the expression for AP is expressed by:

$$AP = \int_0^1 P(R)dR \tag{21}$$

F_{ps} assesses the computational efficiency of the model by quantifying the number of image frames processed per unit time, can be derived from equation (22).

$$F_{ps} = \frac{N}{t} \tag{22}$$

where, T_P is the number of samples with correctly identified defects; F_P is the number of samples with incorrectly identified defects; F_N is the number of samples with undetected defects; n is the number of defect categories; N is the number of samples tested; and t is the total detection time.

To assess the performance of the proposed model in detecting defects in images of HDPE pipe thermal fusion joints, we conducted a comparative analysis against Faster R-CNN, YOLOv5, and YOLOX using the same dataset while maintaining consistent experimental conditions and parameters. The results of this comparison are summarized in Table 2. The findings reveal that the model presented in this paper outperforms the other models in terms of P, R, and mAP indices. Our model achieves a 2.31% improvement in the overall mAP@0.5 compared to the YOLOX model.

[insert **Table 2**]

Table 2 Comparison of detection results of different algorithms

Ablation studies were carried out to ascertain the influence of different enhancement modules on the model's recognition performance. The results of these experiments are presented in Table 3. The findings demonstrate that the incorporation of the Improved YOLOX led to significant improvements in the model's mean average precision at an intersection over union threshold of 0.5. Specifically, the use of the CBAM attention mechanism enhanced the mAP@0.5 by 1.71%, while the adoption of the CIoU loss function resulted in a 0.78% increase compared to the YOLOX model. It is noteworthy that the introduction of these enhancement modules slightly reduced the detection speed due to the increased computational complexity. Nonetheless, the detection rate for thermal fusion joint images of HDPE pipes still meets the industrial requirements, indicating the practical viability of the proposed model.

[insert **Table 3**]

Table 3 Results of ablation experiments

4.4 Practical Verification of the Model Performance

Fig. 10 shows the results of automatic detection of different defects in thermal fusion joints. Images (a) to (c) represent the detection results of the YOLOX model, while (d) to (f) represent the detection results of the improved YOLOX. The figure includes φ2 mm holes (a) and (d) at depths of 10 mm, 16 mm, and 22 mm; grooves (b) and (e) at depths of 3mm by 7.5 mm, and holes (c) and (f) at depths of φ3mm. As shown in Fig. 10(a) and (d), for holes at depths of 10 mm and 22 mm, the improved YOLOX outperformed YOLOX, improving detection accuracy from 0.63 to 0.72 and 0.51 to 0.79 respectively.

Fig. 10(b) and (e) show that the improved YOLOX enhanced recognition accuracy for groove defects. In Fig. 10(c) and (f), the improved YOLOX accurately identified φ3mm hole defects at 16 mm depth, while YOLOX mistakenly identified the bottom wave as a defect. The improved YOLOX model significantly enhanced detection capabilities and identified smaller defects with greater accuracy. The detection rate for irregularly shaped hole defects also improved notably. However, recognition performance for groove defects did not see a significant improvement. This could be due to insufficient data available for training the model on groove defects. Further enhancements to the dataset, especially focusing on groove defects, are warranted.

[insert **Fig. 10**(a)]
[insert **Fig. 10**(b)]
[insert **Fig. 10**(c)]
[insert **Fig. 10**(d)]
[insert **Fig. 10**(e)]
[insert **Fig. 10**(f)]

Fig. 10 Results of automatic detection of different defects in thermal fusion joints. (a)-(c) YOLOX (d)-(f) improved YOLOX.

5 Conclusions

This study has explored TFM imaging and intelligent defect recognition in thermal fusion joints of HDPE pipes. We have been presented a D-CCF-TFM algorithm which takes into account the directivity of the ultrasonic array to reduce structural noise in the detected images, thereby improving the SNR and generating high-quality images suitable for intelligent recognition. Furthermore, we investigated a deep learning-based intelligent defect recognition method utilizing an improved YOLOX network, aiming to enhance the efficiency and accuracy of nondestructive testing. The findings of this research can be summarized as follows:

(1) The proposed D-CCF-TFM algorithm has demonstrated average detection errors of less than 0.74 mm in the defect width dimension and 0.86 mm in the defect depth dimension for HDPE pipe thermal fusion joints. In terms of image SNR, the D-CCF-TFM algorithm produces images with improved overall performance compared to the TFM and CCF algorithms, respectively.

(2) The proposed improved YOLOX model, constructed using a dataset containing 2504 real inspection data points for training, established a defect recognition model for TFM images of HDPE pipe hot-melt joints, which achieved a mAP@0.5 value of 99.15%, which is 2.31% higher than the original YOLOX model. The model produced promising detection results for real defect images (including smaller and irregularly shaped defects).

(3) The defect detection model established in this paper can be used to automatically identify the TFM images of thermal fusion joints, which can significantly improve the detection efficiency of thermal fusion joints in urban gas pipelines and reduce the risk of misjudgment in manual evaluation of images. This is of great significance to ensure the safe and stable operation of the pipeline.

Acknowledgments

Not applicable

Author Contributions

Tianliang Chen: Methodology, software and wrote the main manuscript. QiangWang reviewed the manuscript and provide a great deal of constructive advice. Quanjing Xiao helped with the validation and interpretation of results. Hong Wang and Yanlei Liu Provided materials and resources and participated in manuscript reviews.

Funding

This work was supported by National Key Research and Development Program of the China (No. 2023YFF0611600) and the “Pioneer” and “Leading Goose” R&D Program of Zhejiang Province (No.2022C03179).

Data availability

Data will be made available on request.

Declaration

Ethics approval and consent to participate: Not applicable

Consent for publication: Not applicable.

Competing interest: The authors declare that they have no known competing financial interests or personal relationships that could have appeared to influence the work reported in this paper.

References

[1] Y. Wang, D. Lin, M. Xiang, M. Cui, et al., Experimental Study on Aging Performance of Polyethylene Gas Pipelines, IOP Conf. Ser.: Earth Environ, IOP Conf. ser.: Earth Environ.Sci.631 (1) (2021), 012066.

[2] D. Zhang, M. Nie, Y. Xiang, and W. Yin, Effect of rotation extrusion and molecular weight on ductile failure of polyethylene pipes under hydrostatic pressure, Plast, Rubber Compos. 48 (6) (2019) 263–269.

[3] Plastic Pipe Data Collection (PPDC) Initiative - American Public Gas Association.

[4] M. Saif, Andri Haryono, and M. A. Abou-Khousa, Microwave Non-destructive Evaluation of Glass Reinforced Epoxy and High-Density Polyethylene Pipes, J. Nondestr. Eval. 39 (1) (2020).

[5] R. Kafieh, T. Lotfi, and R. Amirfattahi, Automatic Detection of Defects on Polyethylene Pipe Welding Using Thermal Infrared Imaging, Infrared Phys. Technol 54 (4) (2011) 317–325.

[6] N. Palka, R. Panowicz, Marek Chalimoniuk, and R. Beigang, Non-destructive Evaluation of Puncture Region in Polyethylene Composite by Terahertz and X-ray Radiation, Composites Part B: Engineering 92 (2016) 315–325.

[7] C. Frederick, A. Porter, and D. Zimmerman, High-Density Polyethylene Piping Butt-Fusion Joint Examination Using Ultrasonic Phased Array, J. Press. Vessel Technol 132 (5) (2010),051501.

[8] J. Zheng, D. Hou, W. Guo, X. Miao, Y. Zhou, and J. Shi, Ultrasonic Inspection of Electrofusion Joints of Large Polyethylene Pipes in Nuclear Power Plants, J. Press. Vessel Technol 138 (6) (2016),060908.

[9] C. Holmes, B. W. Drinkwater, and P. D. Wilcox, Post-processing of the Full Matrix of Ultrasonic Transmit–Receive Array Data for Non-destructive Evaluation, NDT & E Int. 38 (8) (2005) 701–711.

[10] E. Lopez Villaverde, S. Robert, and C. Prada, Ultrasonic Imaging in Highly Attenuating Materials with Hadamard Codes and the Decomposition of the Time Reversal Operator, IEEE trans. Ultrason. Ferroelect. Freq. Control 64 (9) (2017) 1336–1344.
[11] Y. Xie, L. Zhou, X. Zhang, J. Wu, and J. Dou, Defect Data Image Enhancement Method Based on All-Focus Imaging Algorithm, Meas. Sci. Technol 33 (11) (2022) ,115402.
[12] J. Camacho and C. Fritsch, Phase Coherence Imaging of Grained Materials, IEEE Trans. Ultrason. Ferroelectr. Freq. Control 58 (5) (2011) 1006–1015.
[13] J. Pedro, M. Parrilla, and C. Fritsch, Phase Coherence Imaging, IEEE Trans. Ultrason. Ferroelectr. Freq. Control, 56 (5) (2009) 958–974.
[14] L. Ge, Z. Wang, Q. Li, C. Lu, and H. Wan, High-Resolution Ultrasonic Imaging Technology for the Damage of Concrete Structures Based on Total Focusing Method, Comput. Electr. Eng. 105 (2023),108526.
[15] J. Tian, Z. Chen, S. Lu, X. Qi, S. Pu, and M. Liu, Phase Coherence Weighted Ultrasound Total Focus Method Towards the Improved Imaging of CFRP Defect," Compos. Commun, 43 (2023),101736.
[16] J. Camacho, D. Atehortua, J. F. Cruza, J. Brizuela, and J. L. Ealo, Ultrasonic Crack Evaluation by Phase Coherence Processing and TFM and Its Application to Online Monitoring in Fatigue Tests, NDT & E Int. 93 (2018) 164–174.
[17] B. Gauthier, G. Painchaud-April, A. Le Duff, and P. Bélanger, Ultrasonic Multi-View Data Merging Using the Vector Coherence Factor, NDT & E Int. 136 (2023),102805.
[18] W.-F. Zhu, Y. Xiang, H. Zhang, Y. Cheng, G. Fan, and H. Zhang, Research on Ultrasonic Sparse DC-TFM Imaging Method of Rail Defects, Meas. 200 (2022),111690.
[19] H. Hu, J. Du, N. Xu, H. Jeong, and X. Wang, Ultrasonic Sparse-TFM Imaging for a Two-Layer Medium Using Genetic Algorithm Optimization and Effective Aperture Correction, NDT & E Int. 90 (2017) 24–32.
[20] S. Cantero-Chinchilla, P. D. Wilcox, and A. J. Croxford, Deep Learning in Automated Ultrasonic NDE – Developments, Axioms and Opportunities, NDT & E Int. 131 (2022) 102703.
[21] H. Sun, P. Ramuhalli, and R. E. Jacob, Machine Learning for Ultrasonic Nondestructive Examination of Welding Defects: A Systematic Review, Ultrasonics 127 (2023),106854.
[22] Mostafa Hasanian, M. Ramezani, Behnoush Golchinfar, and Hossain Saboonchi, Automatic Segmentation of Ultrasonic TFM Phased Array Images: The Use of Neural Networks for Defect Recognition, Proc. SPIE (2020),113790.
[23] Cong Li, Hui-Qing Lan, Ya-Nan Sun, and Jun-Qiang Wang, Detection Algorithm of Defects on Polyethylene Gas Pipe Using Image Recognition, Int. J. Press. Vess. Pip. 191 (2021),104381.
[24] D. Medak, Luka Posilović, M. Subasić, M. Budimir, and S. Lončarić, Automated Defect Detection from Ultrasonic Images Using Deep Learning, IEEE Trans. Ultrason. Ferroelectr. Freq. Control, 68 (10) (2021) 3126–3134.
[25] L. Posilović, D. Medak, M. Subasić, T. Petković, M. Budimir, and S. Lončarić, Flaw Detection from Ultrasonic Images Using YOLO and SSD, ISPA. (2019) 163-168.
[26] T. Gantala and K. Balasubramaniam, Automated Defect Recognition for Welds Using Simulation Assisted TFM Imaging with Artificial Intelligence, J. Nondestr. Eval. 40 (1) (2021),28.
[27] Y. Tao, J. Shi, W. Guo, and J. Zheng, Convolutional Neural Network Based Defect Recognition Model for Phased Array Ultrasonic Testing Images of Electrofusion Joints, J. Press. Vessel Technol 145 (2) (2023),024502.
[28] Z. Ge, S. Liu, F. Wang, Z. Li, and J. Sun,YOLOX: Exceeding YOLO Series in 2021, arXiv:2107.08430, (2021).
[29] S. Ren, K. He, R. Girshick, and J. Sun, Faster R-CNN: Towards Real-Time Object Detection with Region Proposal Networks, IEEE Trans. Pattern Anal. Mach. Intell. 39 (6) (2017) 1137–1149.
[30] Z. Zheng, P. Wang, W. Liu, J. Li, R. Ye, and D. Ren, Distance-IoU Loss: Faster and Better Learning for Bounding Box Regression, Proc. AAAI Conf. Artif. Intell. 34 (7) (2020) 12993–13000.

Fig and Table

Fig. 1

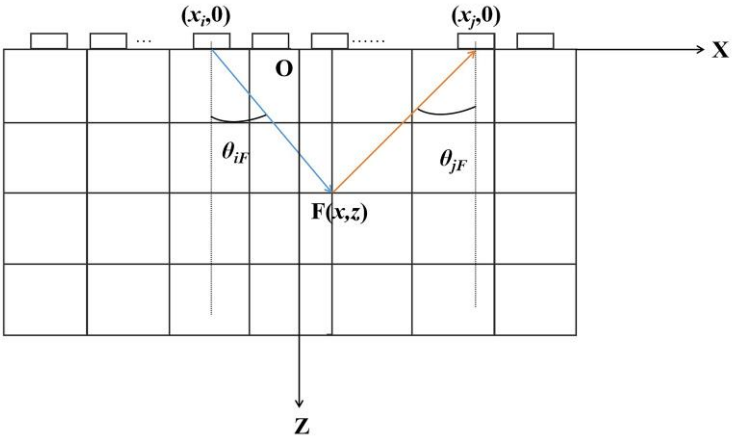


Fig. 2

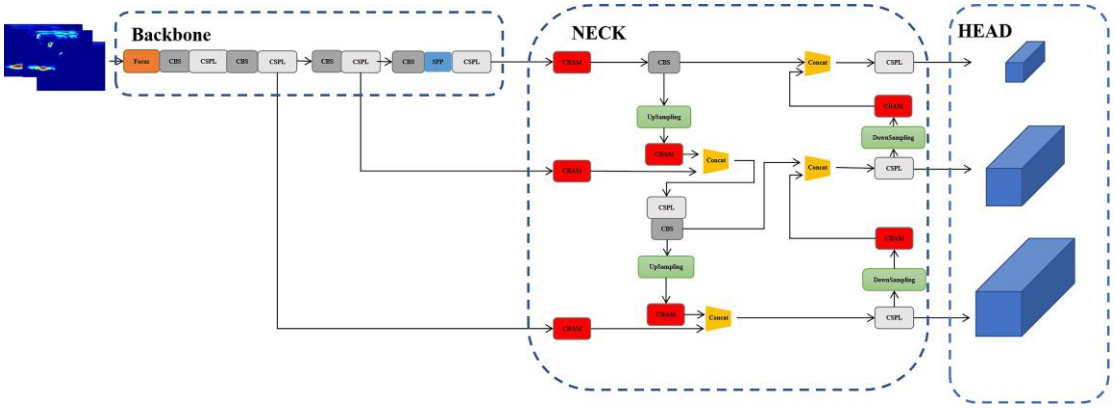


Fig. 3(a)

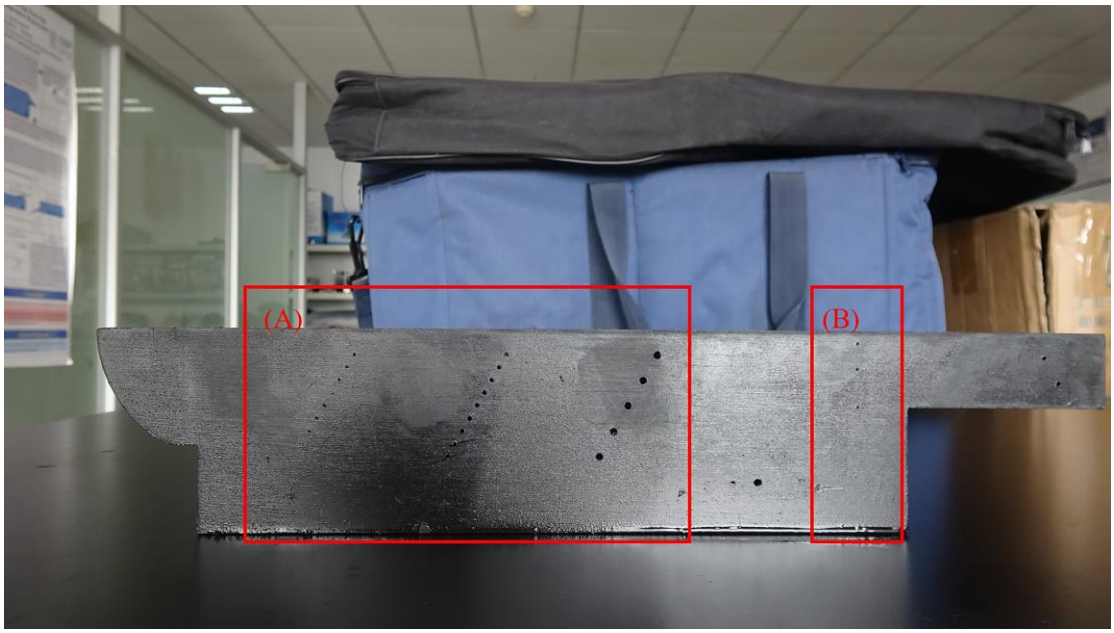


Fig. 3(b)



Fig. 3(c)



Fig. 4

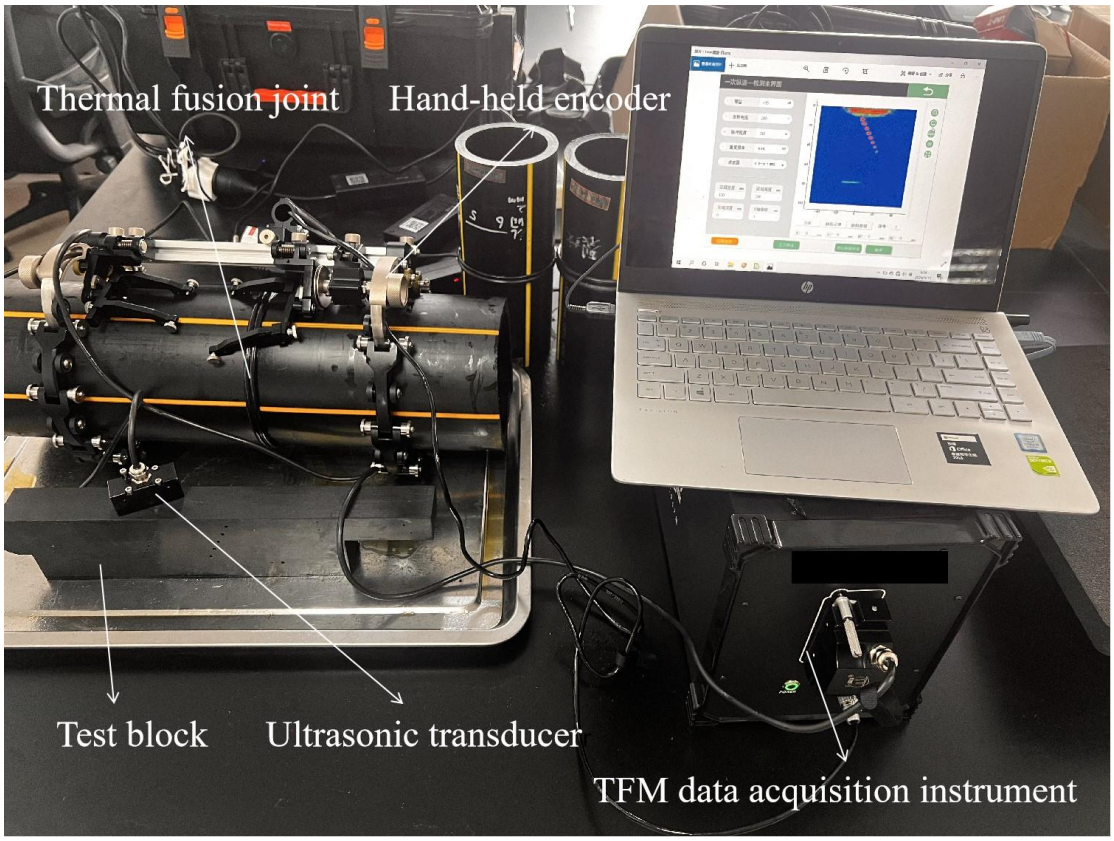

Thermal fusion joint
Hand-held encoder
Test block
Ultrasonic transducer
TFM data acquisition instrument

Fig. 5(a)

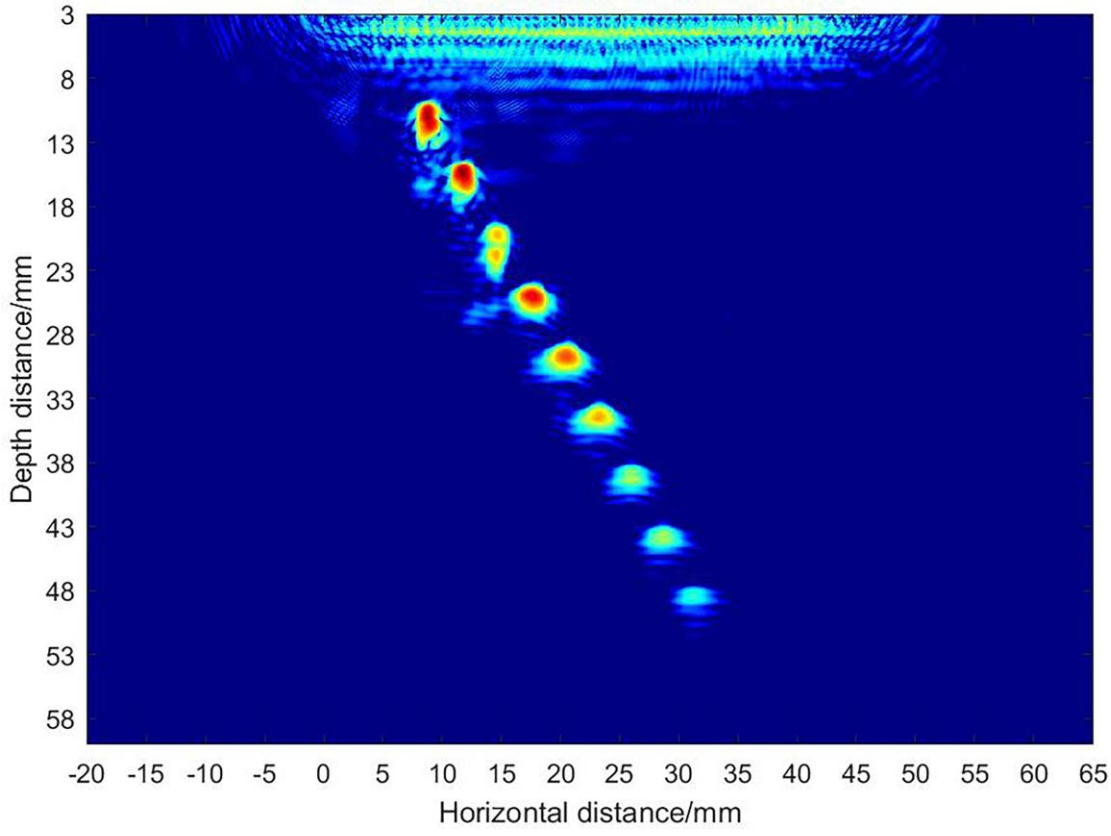

Depth distance/mm
3
8
13
18
23
28
33
38
43
48
53
58
-20 -15 -10 -5 0 5 10 15 20 25 30 35 40 45 50 55 60 65
Horizontal distance/mm

Fig. 5(b)

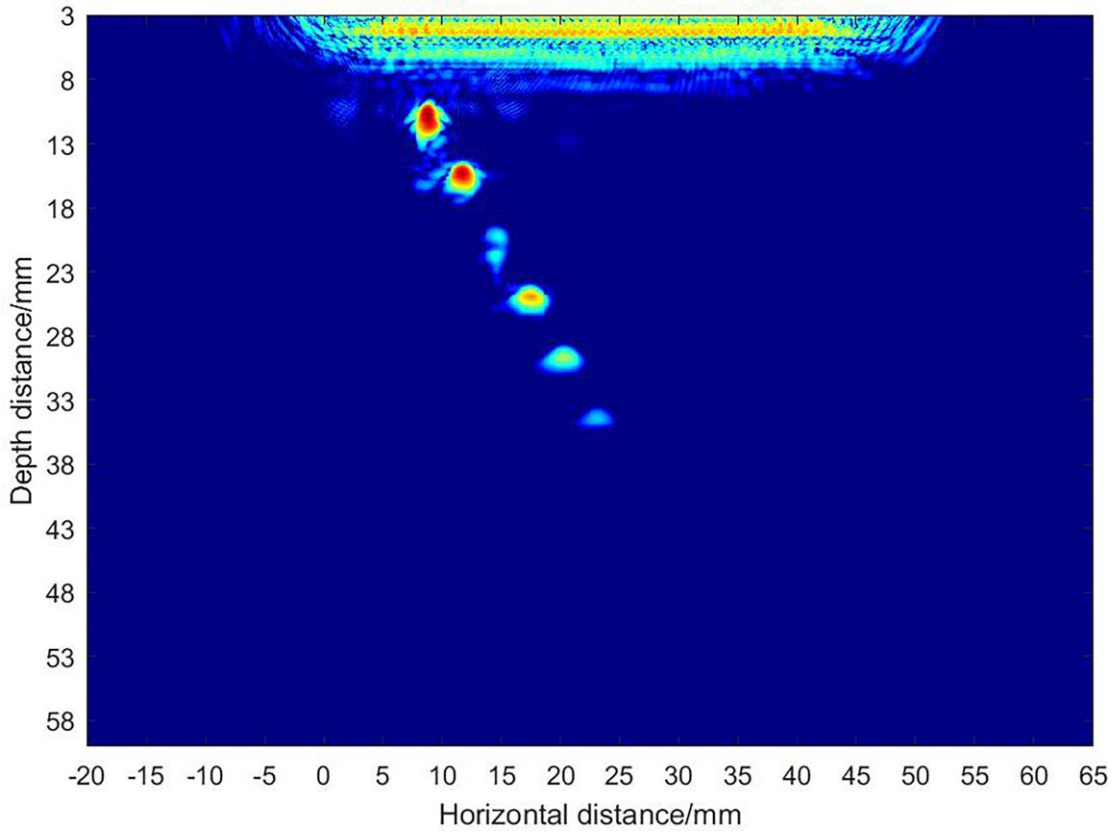

Depth distance/mm
3
8
13
18
23
28
33
38
43
48
53
58
-20 -15 -10 -5 0 5 10 15 20 25 30 35 40 45 50 55 60 65
Horizontal distance/mm

Fig. 5(c)

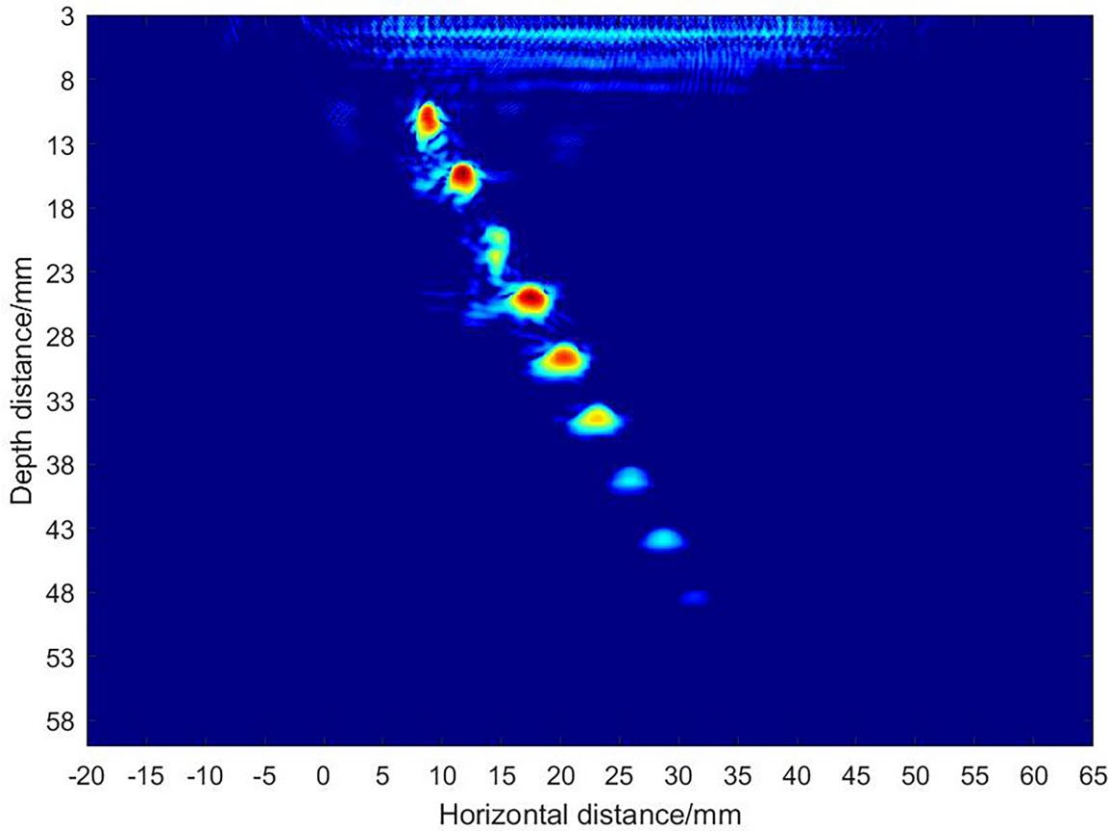

Depth distance/mm
3
8
13
18
23
28
33
38
43
48
53
58
-20 -15 -10 -5 0 5 10 15 20 25 30 35 40 45 50 55 60 65
Horizontal distance/mm

Fig. 6(a)

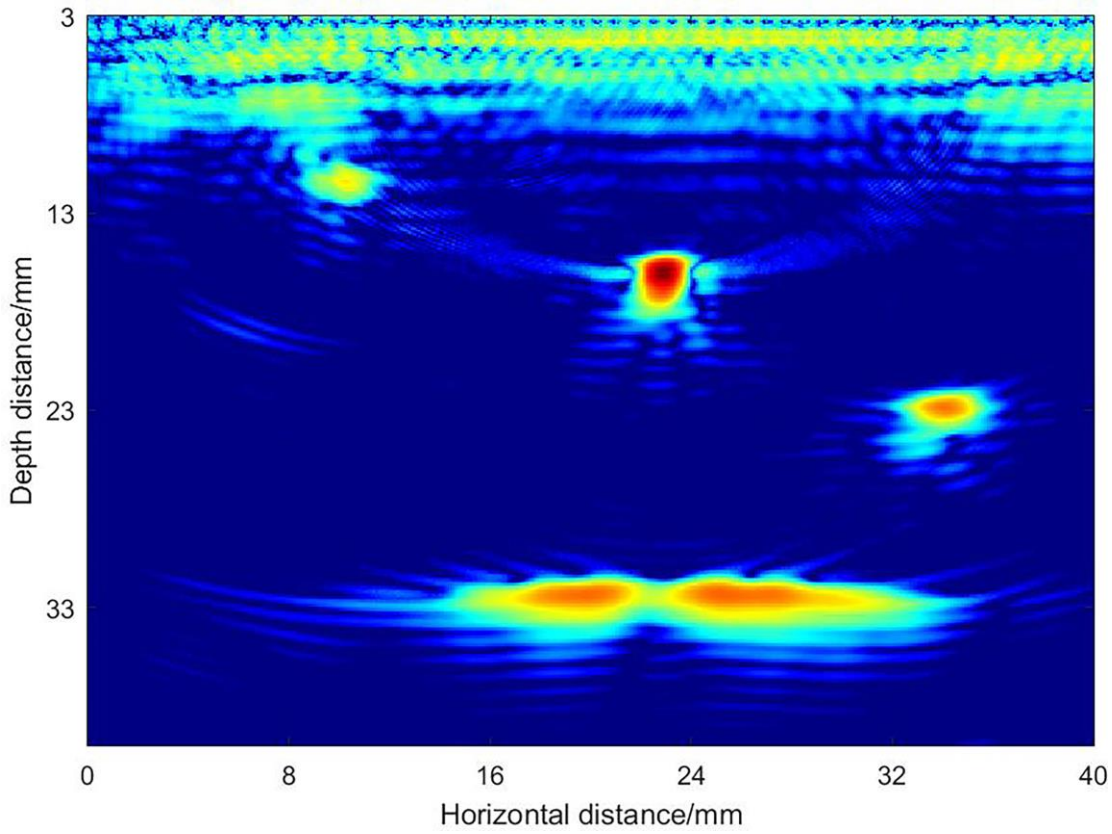

3
13
23
33
Depth distance/mm
0
8
16
24
32
40
Horizontal distance/mm

Fig. 6(b)

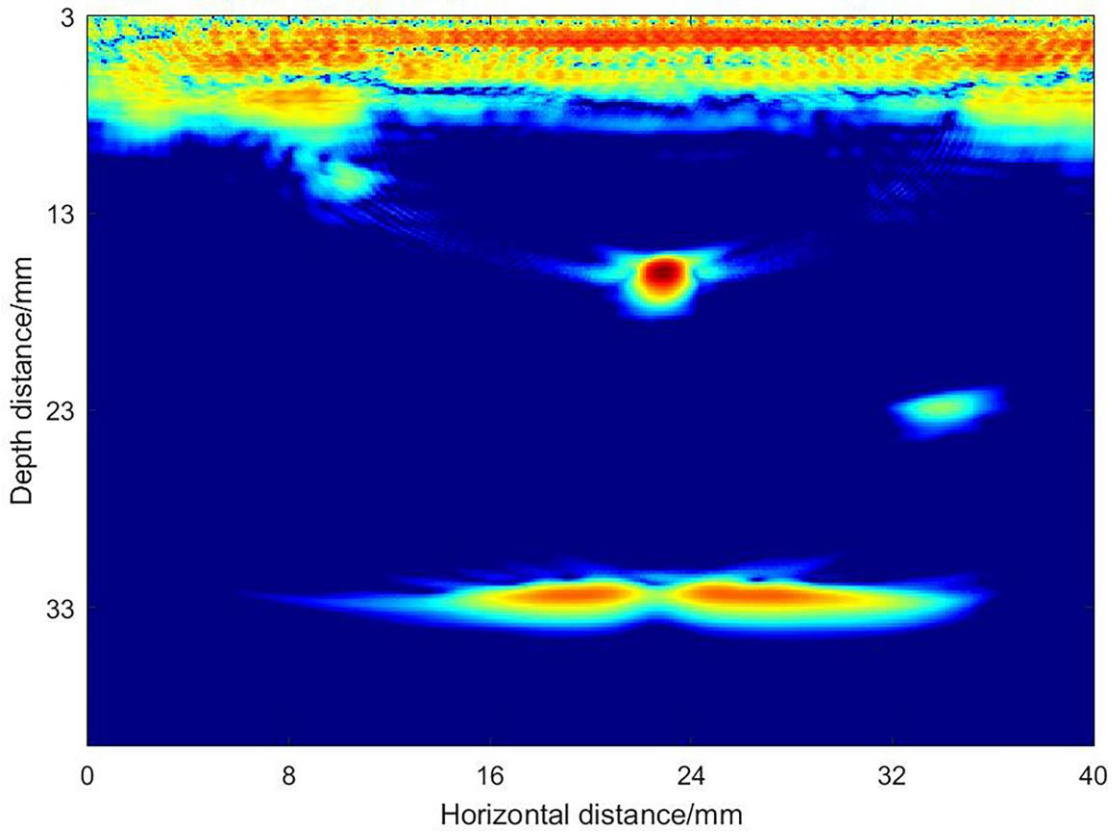

3
13
23
33
Depth distance/mm
0
8
16
24
32
40
Horizontal distance/mm

Fig. 6(c)

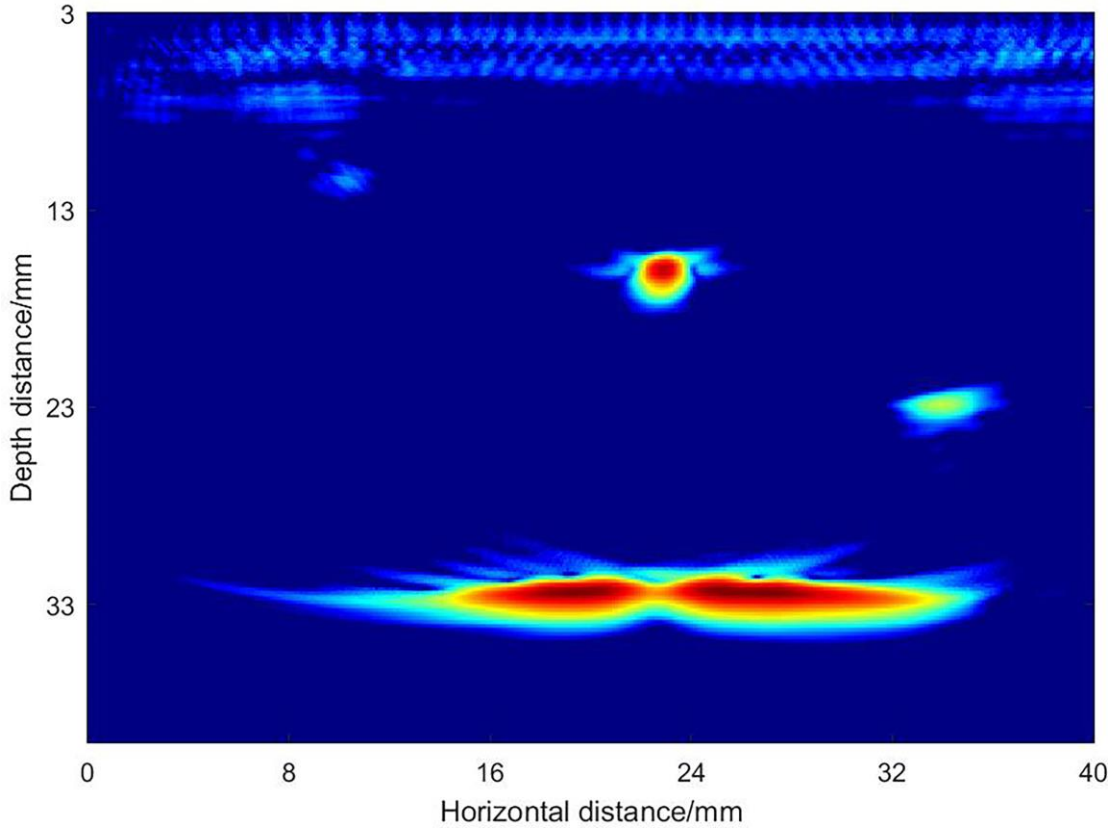

3
13
23
33
Depth distance/mm
0
8
16
24
32
40
Horizontal distance/mm

Fig. 7(a)

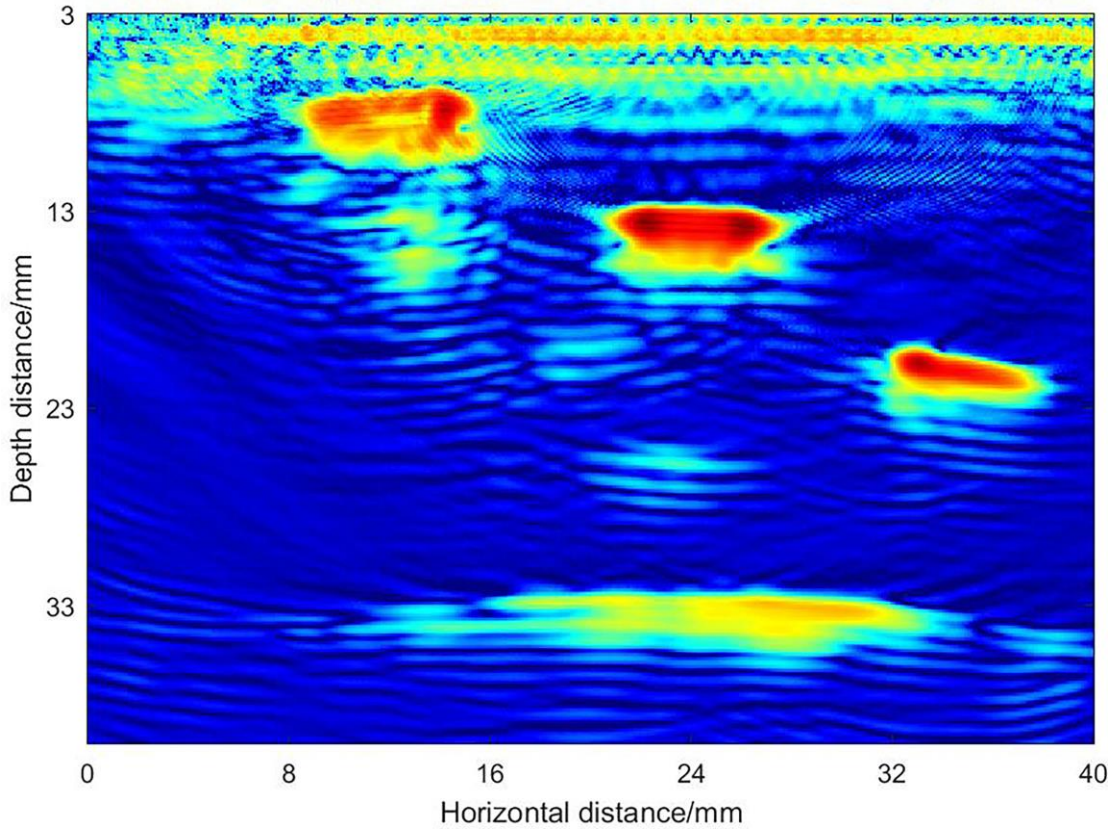

3
13
23
33
Depth distance/mm
0
8
16
24
32
40
Horizontal distance/mm

Fig. 7(b)

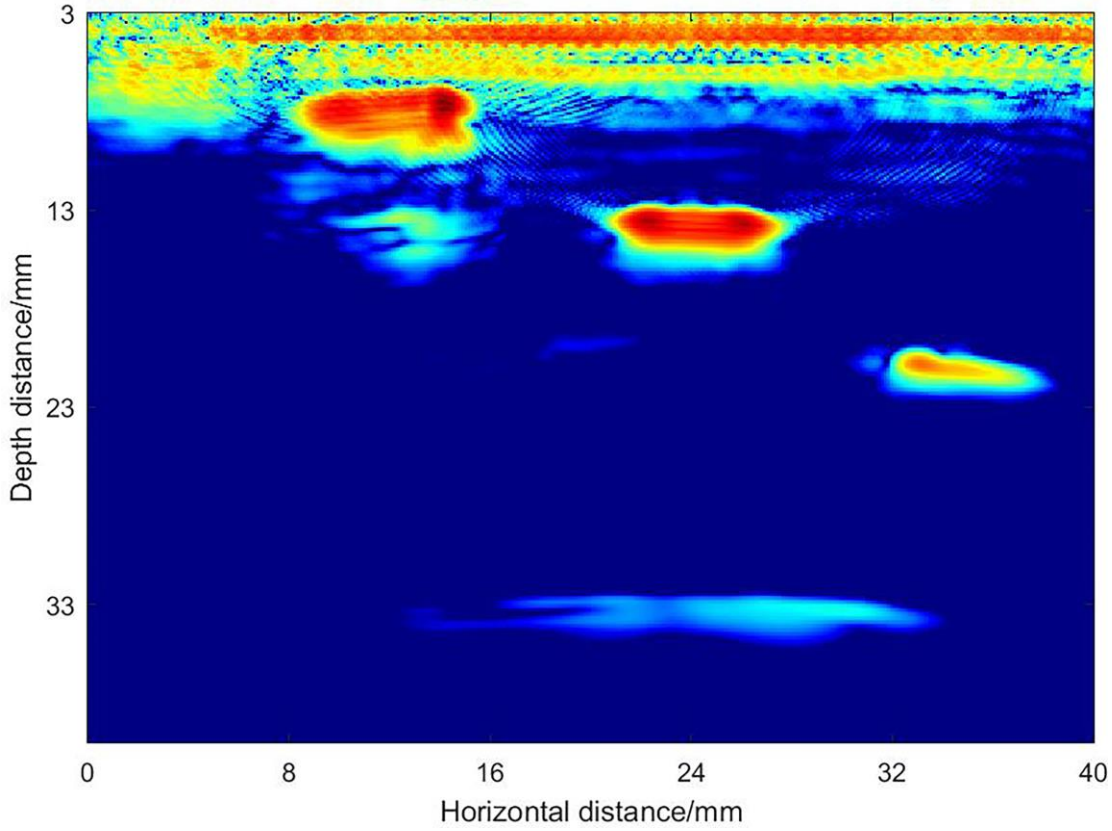

3
13
23
33
Depth distance/mm
0
8
16
24
32
40
Horizontal distance/mm

Fig. 7(c)

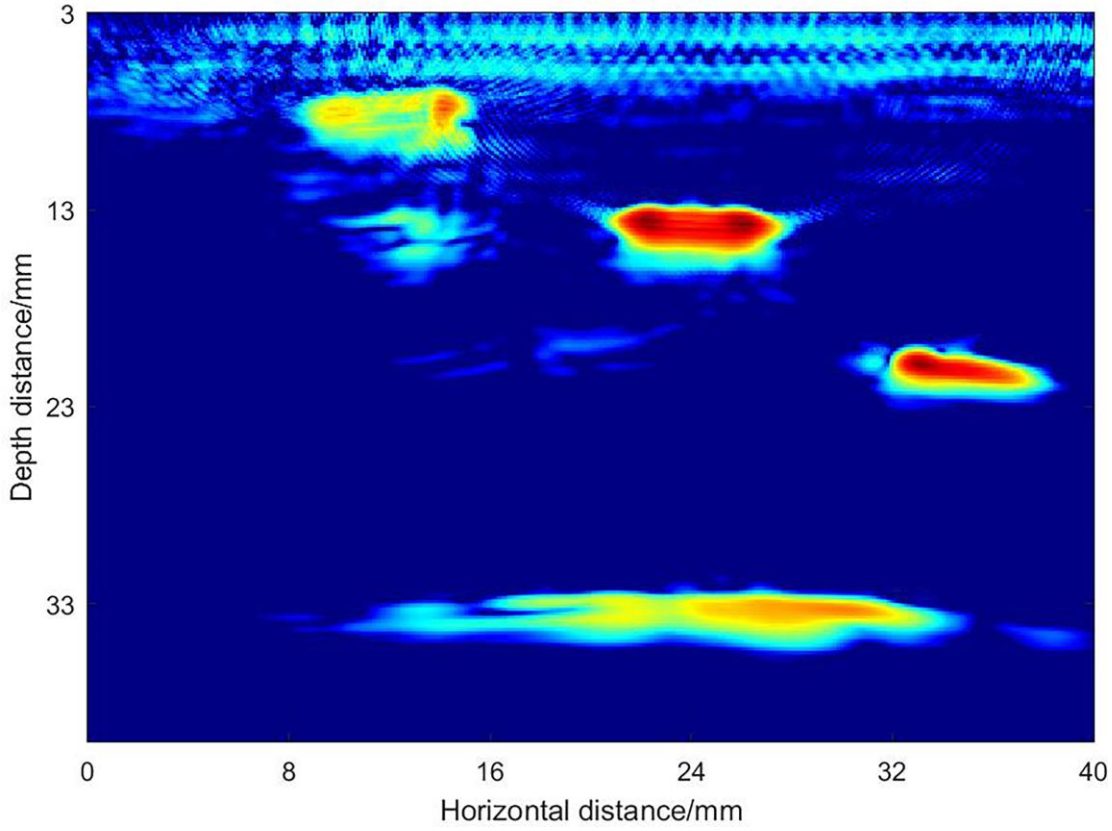

3
13
23
33
Depth distance/mm
0
8
16
24
32
40
Horizontal distance/mm

Fig. 8(a)

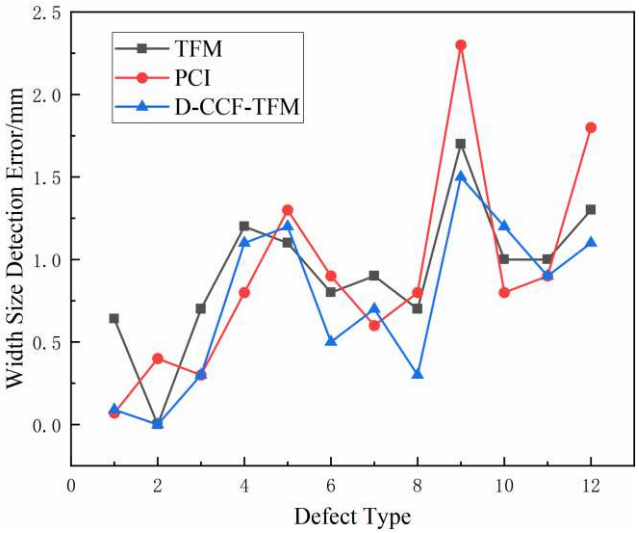

TFM
PCI
D-CCF-TFM
Width Size Detection Error/mm
Defect Type
0.0
0.5
1.0
1.5
2.0
2.5
0
2
4
6
8
10
12

Fig. 8(b)

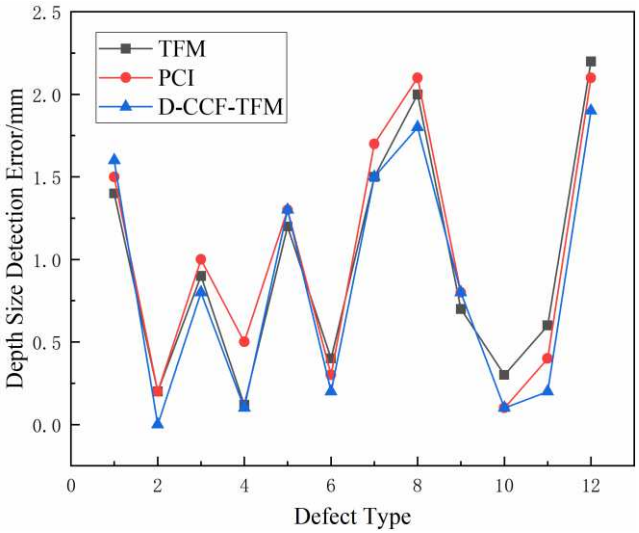

TFM
PCI
D-CCF-TFM
Depth Size Detection Error/mm
Defect Type
0.0
0.5
1.0
1.5
2.0
2.5
0
2
4
6
8
10
12

Fig. 8(c)

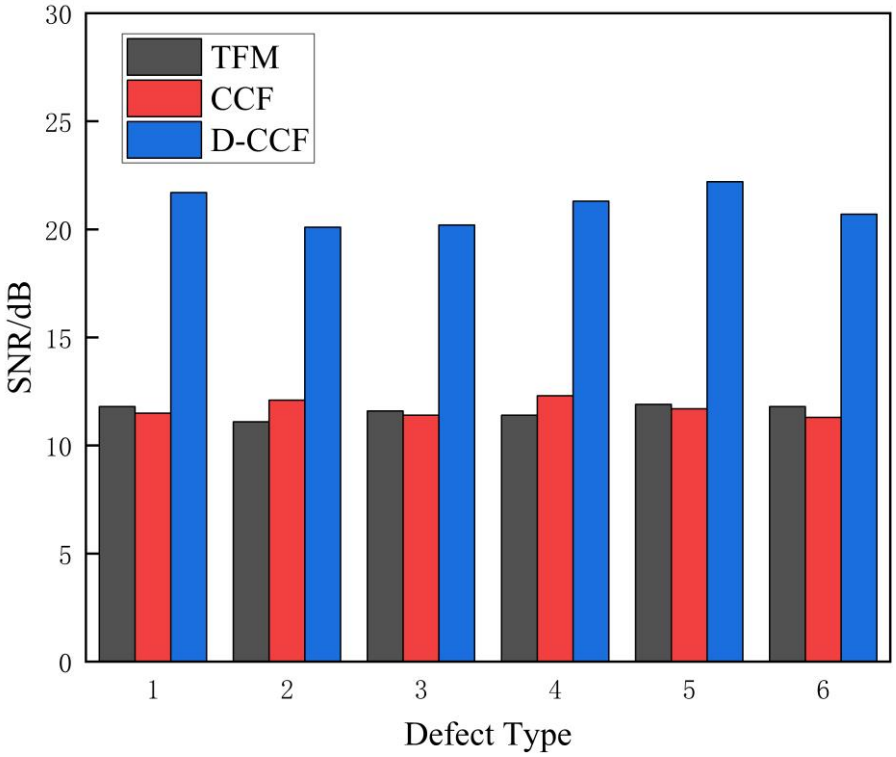

TFM
CCF
D-CCF
SNR/dB
Defect Type
0
5
10
15
20
25
30
1
2
3
4
5
6

Fig. 8(d)

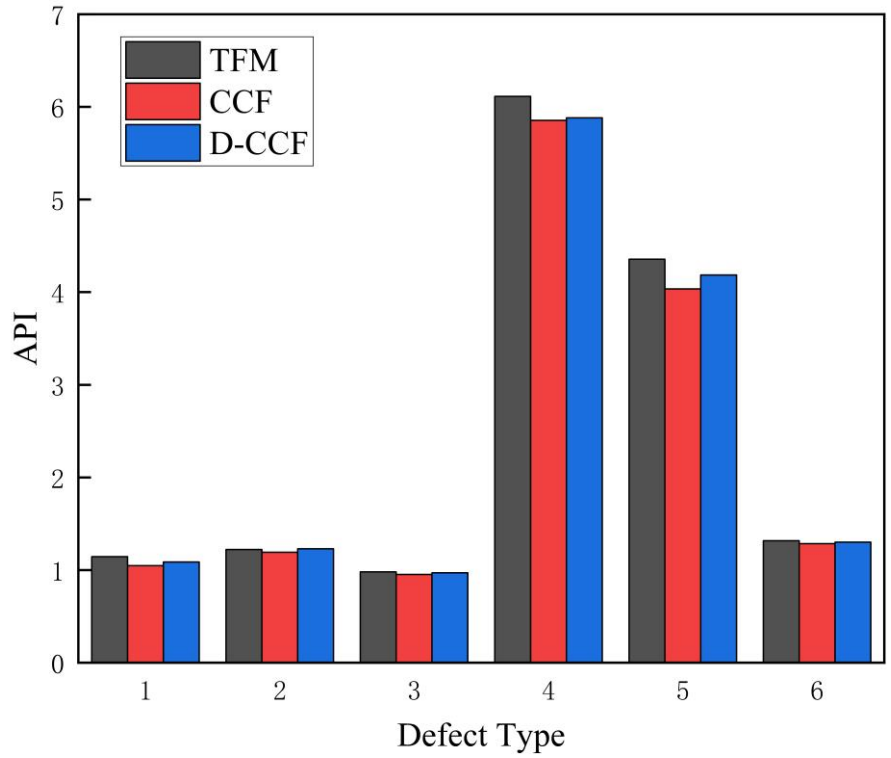

TFM
CCF
D-CCF
API
Defect Type
0
1
2
3
4
5
6
7
1
2
3
4
5
6

Fig. 9(a)

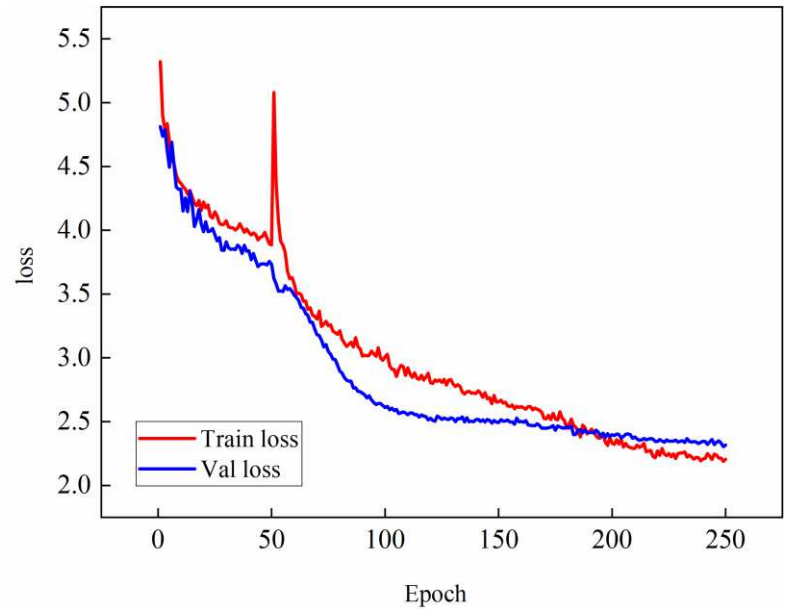

5.5
5.0
4.5
4.0
3.5
3.0
2.5
2.0
loss
Train loss
Val loss
0
50
100
150
200
250
Epoch

Fig. 9(b)

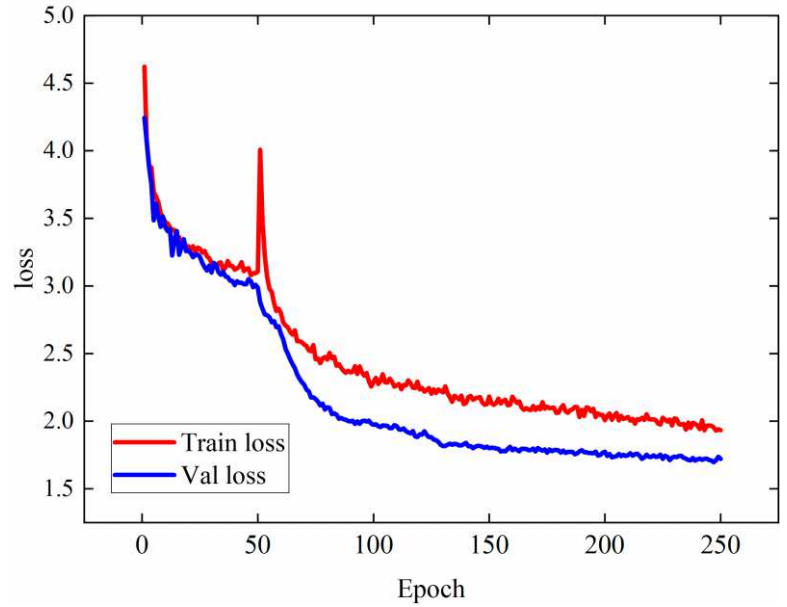

5.0
4.5
4.0
3.5
3.0
2.5
2.0
1.5
loss
Train loss
Val loss
0
50
100
150
200
250
Epoch

Fig. 10(a)

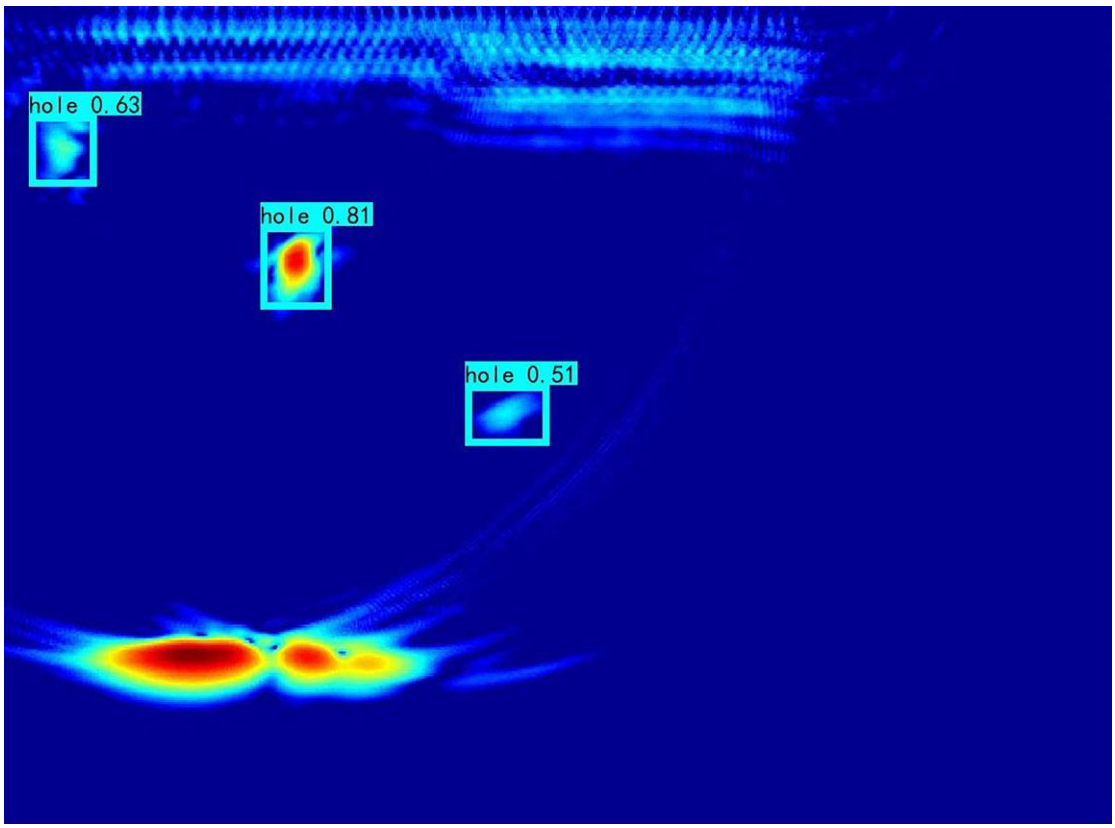


Fig. 10(b)

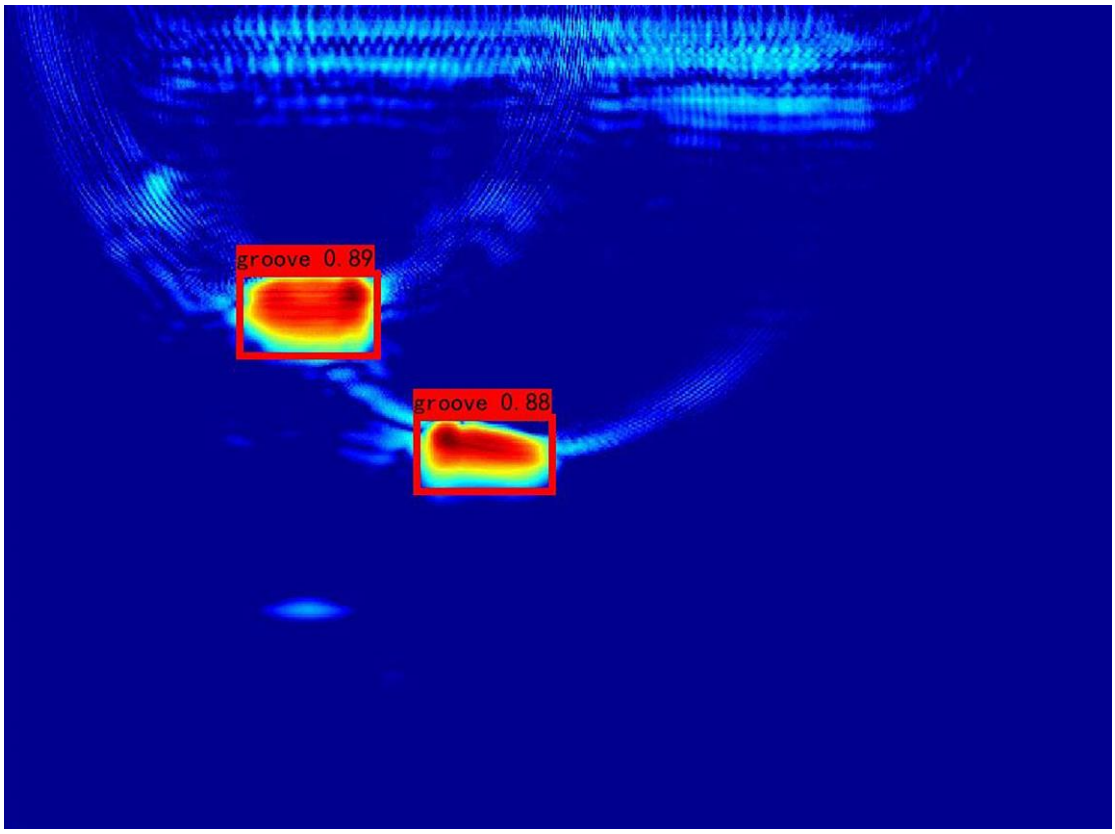


Fig. 10(c)

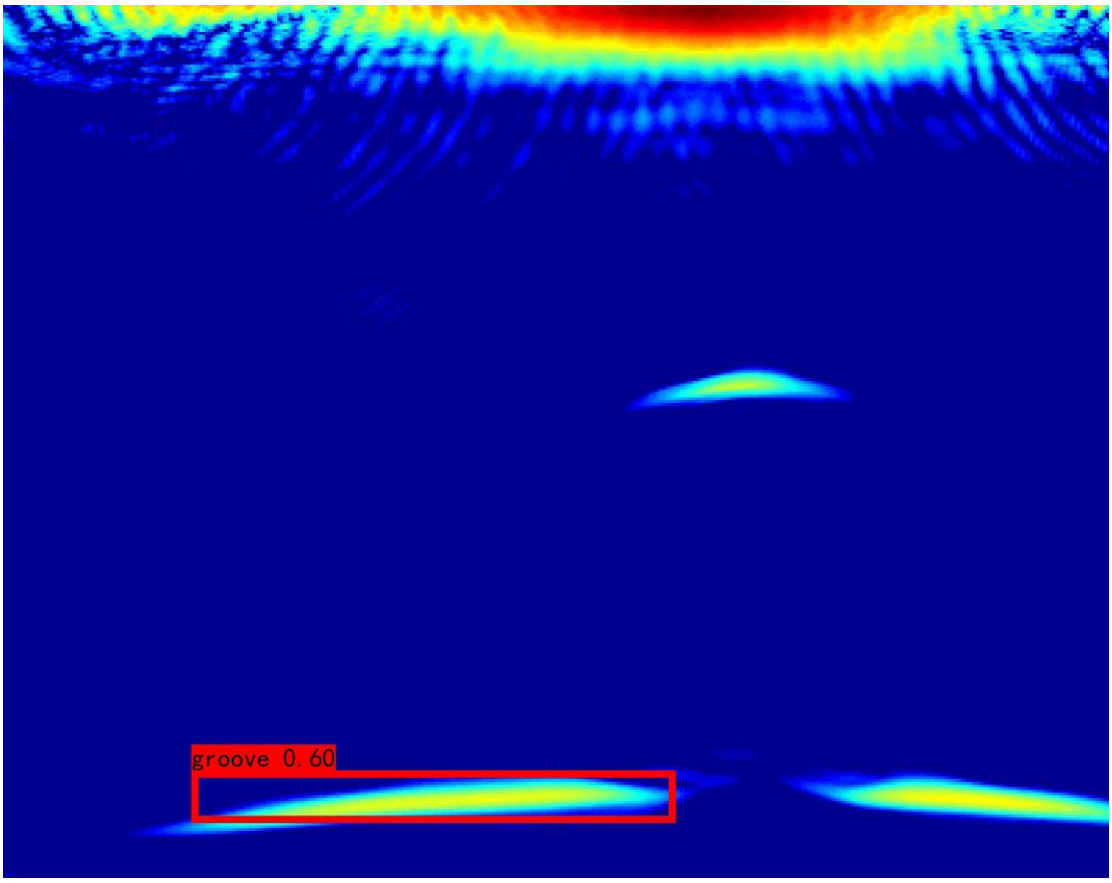


Fig. 10(d)

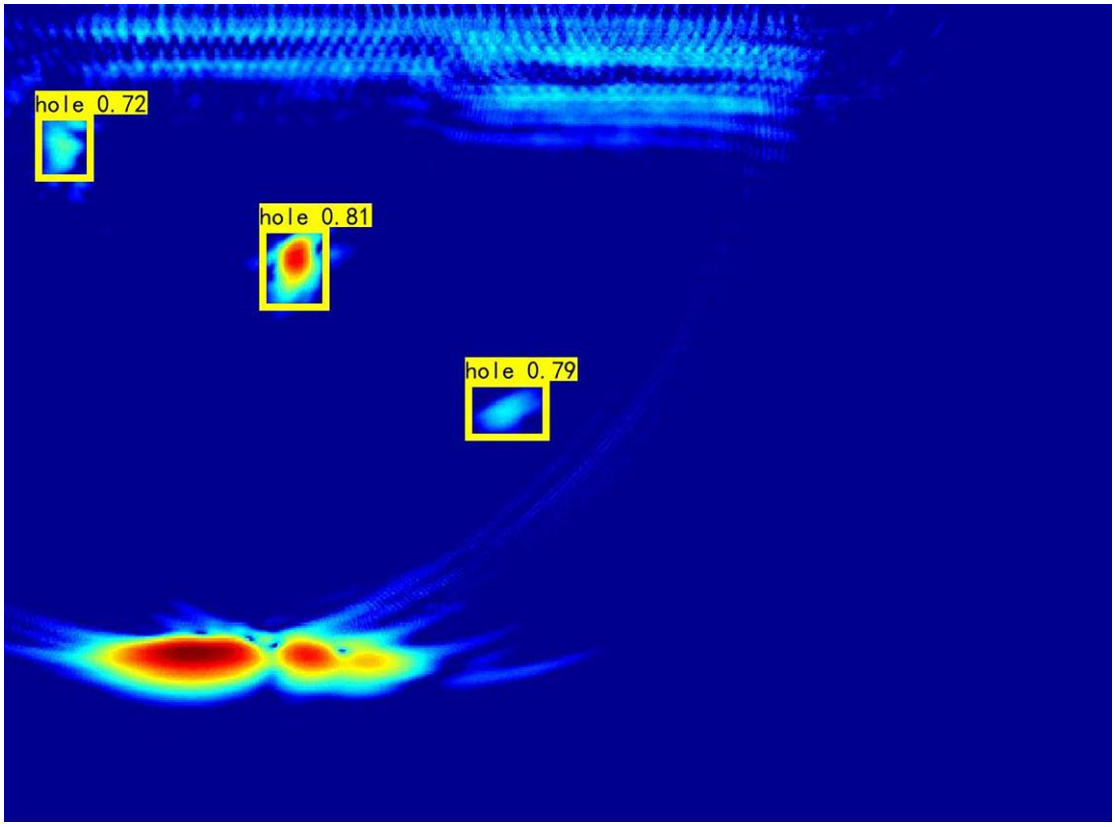


Fig. 10(e)

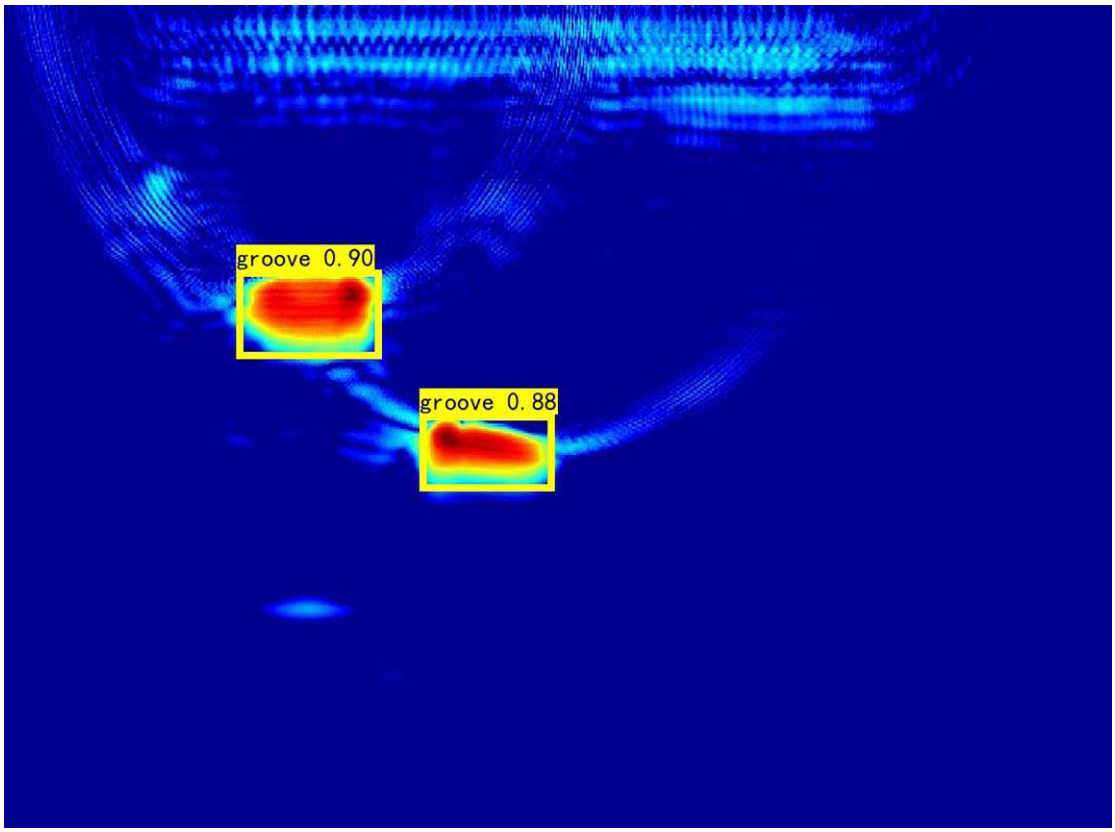


Fig. 10(f)

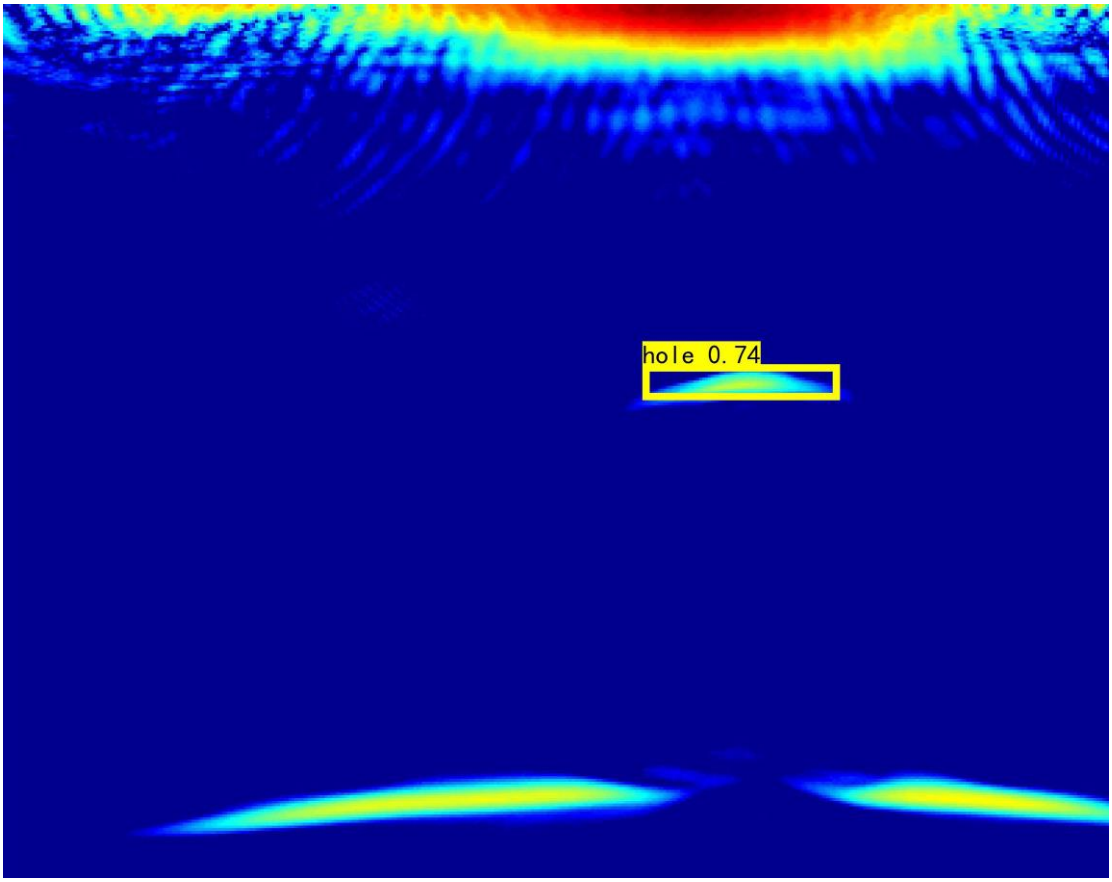


Table 1

Training phase	Epoch	Learning rate	Batch size	Optimizer type	Momentum
Freezing phase	50	0.01	8	SGD	0.937
Unfreezing phase	200	0.0001	4	SGD	0.937

Table 2

Model	P	R	mAP@0.5	F_{PS}
Faster R-CNN	68.67%	85.01%	80.25%	7.53
YOLOv5	87.82%	90.11%	93.43%	11.12
YOLOX	91.99%	96.16%	96.84%	13.74
Improved YOLOX	97.02%	98.40%	99.15%	12.76

Table 3

Group	CBAM	CIoU	mAP@0.5	F_{PS}
1	√		98.55%	12.88
2		√	97.62%	13.30
3			96.84%	13.74

Supplementary Files

This is a list of supplementary files associated with this preprint. Click to download.

- Highlights.doc